RSC Advances

PAPER

View Article Online
View Journal | View Issue

Cite this: *RSC Adv.*, 2025, **15**, 23103

Direct conversion of methane to value-added hydrocarbons using alkali metal-promoted cobalt catalysts†

Sarannuch Sringam,[ab] Punyanut Thansiriphat,[a] Thongthai Witoon,[ab] Waleeporn Donphai,[a] Metta Chareonpanich,[ab] Chularat Wattanakit,[c] Hiesang Sohn,[d] Nevzat Yigit,[e] Günther Rupprechter[e] and Anusorn Seubsai*[ab]

The oxidative coupling of methane (OCM) is a promising pathway for directly converting methane into higher hydrocarbons (C_{2+}). This research investigated the influence of alkali metal promoters (Li, Na, K, or Rb) on Co/Al_2O_3 catalysts prepared based on incipient wetness impregnation for the OCM reaction. The catalyst investigations demonstrated that the catalysts promoted with K and Rb had superior performance, with the 4.6K–Co/Al_2O_3 catalyst achieving a maximum C_{2+} yield of 8.1%, C_{2+} selectivity of 24.0%, and CH_4 conversion of 32.1% at 640 °C. Catalyst characterization, based on XRD, HR-TEM, BET, XPS, CO_2-TPD, and H_2-TPR analyses, revealed the structural and physicochemical properties responsible for the enhanced catalytic activity. Specifically, K and Rb promoters increased surface basicity and enhanced the electron density of active sites, thereby promoting selective methane activation. *In-situ* DRIFTS and mechanistic studies highlighted the role of reactive oxygen species in promoting C_{2+} hydrocarbon formation. These results should position K–Co/Al_2O_3 as a promising catalyst for OCM and provide valuable guidance for designing more efficient catalytic systems for methane utilization.

Received 7th April 2025
Accepted 30th June 2025

DOI: 10.1039/d5ra02408k

rsc.li/rsc-advances

1. Introduction

Methane (CH_4) and carbon dioxide (CO_2) are the most potent greenhouse gases driving global warming and climate change.[1] Methane, in particular, has a global warming potential approximately 25 times greater than CO_2 over a 100 year period, making it a critical target for emission reduction and alternative utilization strategies.[2] Despite its environmental impact, methane is also a valuable raw material for producing more complex and economically essential compounds. Efficient conversion of methane into higher-value chemicals can provide a dual benefit of mitigating climate impact and creating valuable products.[3]

Methane conversion can proceed through two primary pathways: indirect and direct.[4] Indirect routes involve a two-step process, where methane is first reformed (*via* steam reforming, dry reforming, or partial oxidation) to produce syngas, a mixture of hydrogen (H_2) and carbon monoxide (CO). Then, these syngas can be transformed into valuable chemicals, such as olefins and fuels, through processes such as Fischer–Tropsch synthesis. However, the indirect pathway is energy-intensive and requires multiple stages, driving interest toward more efficient direct conversion approaches.[5]

Direct methane conversion aims to simplify the process by producing valuable chemicals in a single step. Such methods include partial oxidation to formaldehyde and methanol or converting methane to higher hydrocarbons (C_{2+}), such as ethylene (C_2H_4), ethane (C_2H_6), propylene (C_3H_6), propane (C_3H_8), and butanes (C_4H_{10}), *via* oxidative coupling of methane (OCM)[6] or non-oxidative coupling of methane (NOCM). Although the NOCM process offers a promising route to convert methane without oxygen, it involves considerable thermodynamic challenges and requires high energy input, limiting its industrial viability.[7,8] Consequently, OCM has attracted substantial attention as a feasible pathway for directly converting methane to C_{2+}. In the OCM process, methane reacts with molecular oxygen at high temperatures (above 700 °C) to produce these valuable compounds and byproducts, including water, hydrogen, carbon monoxide, and carbon dioxide.[9]

Early research on OCM explored a range of catalysts, including pure oxides of rare earth, alkaline earth, and transition metals.[10] However, the focus has shifted towards more sophisticated catalyst formulations to enhance methane

[a]*Department of Chemical Engineering, Faculty of Engineering, Kasetsart University, Bangkok 10900, Thailand. E-mail: fengasn@ku.ac.th*
[b]*Center of Excellence on Petrochemical and Materials Technology, Kasetsart University, Bangkok 10900, Thailand*
[c]*School of Energy Science and Engineering, Vidyasirimedhi Institute of Science and Technology, Rayong 21210, Thailand*
[d]*Department of Chemical Engineering, Kwangwoon University, Seoul, 01897, South Korea*
[e]*Institute of Materials Chemistry, Technische Universität Wien, Vienna 1060, Austria*

† Electronic supplementary information (ESI) available. See DOI: https://doi.org/10.1039/d5ra02408k

conversion and selectivity toward higher hydrocarbons. Among the most extensively studied catalysts is Na_2WO_4–Mn/SiO_2,[11,12] which, despite its promising activity, has not been commercialized due to low C_{2+} yield and selectivity, coupled with issues of catalyst deactivation during prolonged operation.[13,14] Challenges, such as sintering, phase changes, and coking, continue to limit the catalyst's industrial applicability, emphasizing the need for innovations that enhance performance and long-term stability.[6]

In 2023, we introduced a novel hybrid catalyst system for the direct conversion of CH_4 to C_{2+}, combining 15 wt% Ni supported on Al_2O_3 ($15Ni/Al_2O_3$) and 20 wt% Co supported on Al_2O_3 doped with 4.6 wt% K ($4.6K–20Co/Al_2O_3$). Operating at relatively low temperatures (490 °C), this catalyst demonstrated impressive results, achieving C_{2+} yields of 3.6–4.3%, with selectivity ranging from 7.9% to 15.8% and CH_4 conversion rates between 27.2% and 46.3%.[15,16] When compared to the individual catalysts under identical conditions, the hybrid catalyst outperformed both, showcasing the synergistic effect of combining Ni and K-promoted Co catalysts. Notably, the $4.6K–20Co/Al_2O_3$ catalyst produced exceptionally high catalytic activity for methane conversion to C_{2+}, whereas the unpromoted $20Co/Al_2O_3$ catalyst was essentially inactive, yielding 0% C_{2+} products. This highlighted the crucial role of K as a promoter in facilitating the direct activation of CH_4—a finding that warranted further investigation.

The selection of appropriate promoters is crucial for addressing the limitations of traditional OCM catalysts. When integrated into the catalyst, alkali metals function as modifiers that enhance the surface basicity.[17] This modulation of catalytic properties can redirect reaction pathways, promoting the formation of higher hydrocarbons (C_{2+}).[18] However, comprehensive studies that have systematically compared the effects of various alkali metals on cobalt-based catalysts have not been explored. In refining catalyst designs, it is crucial to understand how different alkali metal promoters influence the catalyst structure, activity, and selectivity.

Given that K belongs to the alkali metals group, which also includes lithium (Li), sodium (Na), rubidium (Rb), and cesium (Cs), it raises the intriguing possibility that other alkali metals may produce similar effects when used as promoters. Therefore, in this study, we explored the influence of various viable alkali metals (Li, Na, K, and Rb) on the performance of $20Co/Al_2O_3$ catalysts in the OCM reaction. We systematically investigated how these promoters impacted catalytic activity, product selectivity, and CH_4 conversion. In addition, we examined the effect of metal loading on optimizing the OCM process. Various advanced characterization techniques were applied to understand the relationships between the physical and chemical properties of the catalysts and their performance, offering insights into the design of more efficient and stable catalysts for direct methane conversion.

2. Experimental

2.1 Catalyst preparation

All the catalysts were prepared using the incipient wetness impregnation method. The Co/Al_2O_3 catalyst was promoted with different weights of four alkali metals: Li, Na, K, and Rb. Several metal nitrates were used as precursors, consisting of $LiNO_3$ (99.99%, Sigma-Aldrich), $NaNO_3$ (99.5%, Alfa Aesar), $RbNO_3$ (99%, Alfa Aesar), KNO_3 (99%, Alfa Aesar), and $Co(NO_3)_2 \cdot 6H_2O$ (99%, Alfa Aesar). The support used for all catalysts was γ-Al_2O_3 (denoted as Al_2O_3, with a surface area of 75.32 $m^2\ g^{-1}$, 99.97%, Alfa Aesar). Each metal precursor was dissolved in deionized water as a stock solution in the first step. Then, each solution was dropped onto Al_2O_3. Each mixture was stirred for 1 hour at room temperature before heating and continuously stirring at 90 °C until dry. Each dried sample was ground and calcined at 400 °C for 1 hour at a heating rate of 10 °C min^{-1}. The weight percentage of Co in all catalysts was fixed at 20, while the weight percentage of each promoter was in the range 0.1–10.0, with the balance comprising the weight percentage of the Al_2O_3 support. For example, one catalyst was denoted as $4.6K–Co/Al_2O_3$, representing 4.6wt% K, 20wt% Co, and 75.4wt% Al_2O_3. Thus, there were five catalyst groups studied: $Li–Co/Al_2O_3$, $Na–Co/Al_2O_3$, $K–Co/Al_2O_3$, $Rb–Co/Al_2O_3$, and Co/Al_2O_3.

2.2 Catalyst characterization

The crystalline structure of each sample was identified using X-ray diffractometry (XRD; Rigaku Smart Lab XE, 9 kW), using Cu-Kα radiation at 40 kV and 100 mA, a step size of 0.01°, a scan speed of 3° min^{-1}, and a 2θ range of 10–80°.

The morphology of the samples was observed using high-resolution transmission electron microscopy (HR-TEM; JEM-ARM200F) and a high-angle annular dark-field (HAADF) scanning transmission electron microscopy (TEM) and energy dispersive X-ray spectrometry (EDS) (JEM-ARM200F). The operating voltage for the TEM was 200 kV. Before analysis, each sample was prepared by dispersing it in an ethanol solution for 30 min and dropping it onto a copper TEM grid. Then, it was dried in a chamber filled with nitrogen at room temperature.

The surface area, pore volume, and pore size of each catalyst was determined using a nitrogen-physisorption analyzer (3Flex Physisorption Micrometrics). Before measurement, each sample was degassed overnight at 200 °C to remove moisture and other adsorbed molecules. The Brunauer–Emmett–Teller model was used to calculate the surface area, while the Barrett–Joyner–Halenda model was used to calculate the pore size distribution.

The binding energy of Co in each catalyst was analyzed using X-ray photoelectron spectroscopy (XPS; Kratos Model Axis ultra DLD), with a monochromator (Al Kα) as the X-ray source and beam current of 10 mA, with a voltage of 15 kV. The spectra of Co 2p were collected at a pass energy of 40 eV in steps of 0.1 eV. All spectra were calibrated using the C1s signal of the carbon support material at 284.6 eV.

The surface basicity of the catalyst was analyzed using temperature-programmed desorption of carbon dioxide (CO_2-TPD) using an AutoChem II 2920 (Micromeritics). Each sample (200 mg) was contained in a quartz U-tube and heated to 400 °C under a flow of helium (He) gas for 30 min and cooled to 200 °C. Subsequently, a flow of 10% CO_2 in He gas was applied for

60 min and then purged with He gas until the baseline was stable. Next, it was heated again from 200 to 800 °C (heating rate of 10 °C min^{-1}), and the CO_2 desorbed was detected using a thermal conductivity detector (TCD).

The reducibility of the catalysts was analyzed using temperature-programmed reduction of hydrogen (H_2-TPR) using an AutoChem II 2920 (Micromeritics). Each sample (200 mg) was contained in a quartz U-tube and heated to 150 °C under a flow of argon (Ar) gas for 30 min and cooled to 50 °C. When the baseline was stable, a flow of 10% H_2 in Ar gas was applied, and the temperature was increased to 1000 °C (heating rate of 5 °C min^{-1}). The quantity of H_2 consumption was detected using a TCD.

Thermogravimetry/differential thermal analysis (TG/DTA, PerkinElmer TGA 8000) was performed under atmospheric pressure. Prior to analysis, the samples were dried at 80 °C overnight to eliminate residual moisture. TG/DTA measurements were conducted over a temperature range of 30–800 °C, using a heating rate of 5 °C min^{-1} and N_2 flow rate of 50 mL min^{-1}.

A single-beam infrared spectrometer (Bruker VERTEX 70v FT-IR) coupled with a wide-band mercury-cadmium-telluride detector and a liquid-nitrogen-cooled system was used to perform *in situ* diffuse reflectance infrared Fourier transform spectroscopy (DRIFTS). The catalyst (20 mg) was placed inside a stainless-steel flow cell oven with a CaF_2 window. The catalyst was pretreated at 400 °C under Ar gas with a flow rate of 40 mL min^{-1} for 1 hour, followed by cooling to room temperature. Subsequently, the gas was converted to a $CH_4 : O_2 : N_2$ mixture gas with a 2 : 1 : 4 ratio and a total flow rate of 50 mL min^{-1}, and the temperature was increased to 490 °C at a heating rate of 10 °C min^{-1}, with the spectrum being recorded at 1 min intervals for 30 min. Each spectrum was collected based on 128 scans at a resolution of 4 cm^{-1} over a spectral range of 900–4000 cm^{-1}.

2.3 Catalyst activity testing

Each catalyst (40 mg) was packed between quartz wool in a quartz tube with a diameter of 0.5 cm in a plug flow reactor. The reactant gases, consisting of CH_4 (99.999%, Labgaz) and O_2 (99.999%, Linde), with a $CH_4 : O_2$ ratio of 2 and a total flow rate of 40 mL min^{-1}, were fed to the quartz tube at atmospheric pressure and a reaction temperature of 440−740 °C. The feed gases were controlled using mass flow controllers (Aalborg GFC17). The effluent gases were analyzed using an online gas chromatograph (GC-14A; Shimadzu) equipped with a flame ionization detector to evaluate C_2H_4, C_2H_6, C_3H_6, C_3H_8, C_4H_8, and C_4H_{10} and a TCD was used to assess CO, CO_2, and CH_4. A standard calibration curve of five calibration points was established for each gas, with an *R*-squared value exceeding 0.995. This enabled accurate quantification of the mole of effluent gas. The activity of each catalyst was expressed as $\%CH_4$ conversion, $\%C_{2+}$ selectivity, and $\%C_{2+}$ yield, as shown in eqn (1)–(3), respectively.

$$\%CH_4 \text{ conversion} = \frac{n_{CH_4,in} - n_{CH_4,out}}{n_{CH_4,in}} \times 100 \quad (1)$$

$$\%C_{2+} \text{ selectivity} = \frac{2\left(n_{C_2H_4} + n_{C_2H_6}\right) + 3\left(n_{C_3H_6} + n_{C_3H_8}\right) + 4\left(n_{C_4H_{10}}\right)}{2\left(n_{C_2H_4} + n_{C_2H_6}\right) + 3\left(n_{C_3H_6} + n_{C_3H_8}\right) + 4\left(n_{C_4H_{10}}\right) + n_{CO} + n_{CO_2}} \times 100 \quad (2)$$

$$\%C_{2+} \text{ yield} = \frac{\%CH_4 \text{ conversion} \times \%C_{2+} \text{ selectivity}}{100} \quad (3)$$

where *n* is the number of moles.

Each catalyst testing study was conducted at least three times, and the results were repeatable within 10%. The data were presented as average values except for the catalyst stability test. Furthermore, the catalytic performance data contained less than 5% carbon balance errors.

3. Results and discussion

3.1 Performance of catalysts

The catalytic performance levels of the 20 wt% Co/Al_2O_3 catalysts, both unpromoted and promoted with 4.6 wt% of alkali metals (Li, Na, K, and Rb), were evaluated in a plug flow reactor under reaction conditions of 490 °C and atmospheric pressure. As depicted in Fig. 1, incorporating the different alkali promoters led to considerable variations in catalytic activity, allowing the catalysts to be categorized into two distinct groups based on their performance. Group I comprised 4.6K–Co/Al_2O_3 and 4.6Rb–Co/Al_2O_3, which had superior catalytic activity, while Group II included 4.6Li–Co/Al_2O_3, 4.6Na–Co/Al_2O_3, and the unpromoted Co/Al_2O_3, all of which had comparatively lower performance.

The catalysts in Group I achieved C_{2+} hydrocarbon yields in the range 3.4–6.5%, with C_{2+} selectivity in the range 15.2–22.3%

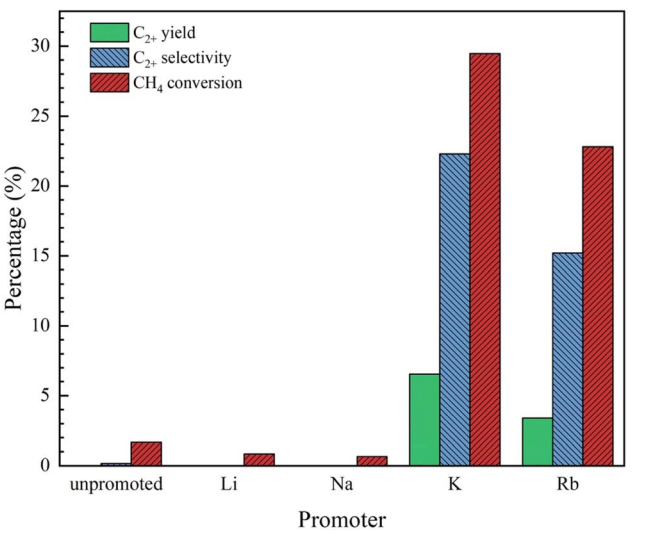

Fig. 1 Catalytic performance of Co/Al_2O_3 catalysts with different promoters for OCM reaction. Reaction conditions: $CH_4 : O_2$ ratio = 2 : 1, catalyst weight = 40 mg, total feed flow rate = 40 mL min^{-1}, reactor temperature = 490 °C.

and CH_4 conversion rates in the range 22.8–29.5%. These results highlighted the enhanced catalytic behavior when K or Rb was used as a promoter. In contrast, the Group II catalysts produced negligible C_{2+} yields (0%) and minimal C_{2+} selectivity (0–0.1%), with CH_4 conversion rates limited to 0.7–1.7%. This stark difference from Group 1 underscored the effectiveness of the K and Rb promoters in enhancing the activity of Co/Al_2O_3 catalysts compared to Li, Na, or no promoter at all.

Based on the results, it was clear that the 4.6K–Co/Al_2O_3 and 4.6Rb–Co/Al_2O_3 catalysts outperformed their counterparts, making them the most promising candidates for further investigation. Consequently, these two catalysts were selected for detailed characterization, as described in Section 3.2, to elucidate the reasons behind their superior catalytic behavior. For comparative purposes, the unpromoted Co/Al_2O_3 catalyst was also characterized to provide a comprehensive analysis of the effects of alkali promotion.

3.2 Catalyst characteristics

3.2.1 Crystal structures of catalyst. The catalysts—Co/Al_2O_3, 4.6K–Co/Al_2O_3, and 4.6Rb–Co/Al_2O_3—were rigorously analyzed using XRD to identify their distinct crystalline phases. Fig. 2 presents the XRD patterns of each catalyst, with the detailed phase information tabulated in Table S1.† Notably, the γ-Al_2O_3 phase appeared consistently across all catalysts, attributed to the identical preparation conditions. Furthermore, for all samples calcined above 250 °C, Co_3O_4 crystallinity was evident, aligning with the known decomposition temperature of $Co(NO_3)_2$ to Co_3O_4.[19] Intriguingly, XRD patterns of the 4.6K–Co/Al_2O_3 catalyst revealed a crystalline KNO_3 phase rather than K_2O, since the transformation to K_2O occurs only beyond 650 °C.[20] In contrast, the 4.6Rb–Co/Al_2O_3 catalyst lacked a discernible crystalline of Rb species, likely due to its amorphous nature or the undetectable crystal size within the XRD sensitivity range.

3.2.2 Catalyst morphology. As illustrated in Fig. 3, the HR-TEM results provided an in-depth look at the morphology of the Co/Al_2O_3, 4.6K–Co/Al_2O_3, and 4.6Rb–Co/Al_2O_3 catalysts. The catalyst particles displayed a variety of irregular shapes and sizes, with dimensions consistently in the range 38–41 nm (see particle size distribution in Fig. S1†). Across all catalysts, the Co_3O_4 particles were dispersed uniformly on the Al_2O_3 support, with the Co_3O_4 (111) crystalline phase having an average *d*-spacing of 0.453–0.462 nm.[21]

In Fig. 4, the HAADF images with EDS elemental mapping reveal a robust elemental distribution of Co, Al, O, K, and Rb. These elements were distributed across all catalysts. Notably, while the crystalline phase of Rb species was undetected in XRD, the HAADF-EDS images distinctly indicate the dispersion of Rb. The even elemental distribution—particularly of the oxygen species—is advantageous for catalytic efficiency in OCM processes.[22]

3.2.3 Physical properties of catalyst. Table 1 summarizes the physical parameters of the catalyst surfaces determined using the N_2-sorption technique. The Co/Al_2O_3 catalyst had a surface area of 60.39 $m^2\ g^{-1}$ and a pore volume of 0.34 $cm^3\ g^{-1}$. After impregnation with K and Rb, these surface properties were reduced due to the deposition of K and Rb within the Al_2O_3 pores. Specifically, the surface area and pore volume of the 4.6K–Co/Al_2O_3 catalyst decreased to 27.80 $m^2\ g^{-1}$ and 0.27 $cm^3\ g^{-1}$, respectively, and for the 4.6Rb–Co/Al_2O_3 catalyst to 46.40 $m^2\ g^{-1}$ and 0.32 $cm^3\ g^{-1}$, respectively. Additionally, Fig. 5 illustrates the variation in pore size. The Co/Al_2O_3 and 4.6Rb–Co/Al_2O_3 catalysts were a bimodal porous material, but the 4.6K–Co/Al_2O_3 was a monomodal porous material, which may occur as a deposit of metal oxides inside the small pores, leading to the loss of one of the pore size regimes. The mean pore diameters of the 4.6K–Co/Al_2O_3 (40.46 nm) and 4.6Rb–Co/Al_2O_3 catalysts (3.49 nm and 44.89 nm) were smaller than that of the Co/Al_2O_3 catalyst (3.71 nm and 47.90 nm), which could be attributed to the presence of K and Rb within the catalyst pores. Furthermore, the N_2 adsorption–desorption isotherm of the catalysts is shown in Fig. 6. According to the International Union of Pure and Applied Chemistry classification, the catalysts exhibited Type IV adsorption isotherms with an H3 hysteresis loop, suggesting that all catalysts were mesoporous materials.[23]

3.2.4. Chemical state of catalysts. Fig. 7 presents the XPS spectra in the Co 2p regions for the catalysts. The Co 2p spectra for all catalysts displayed two distinct regions: at Co $2p_{3/2}$ at lower binding energies (775–790 eV) and Co $2p_{1/2}$ at higher binding energies (790–803 eV), which are characteristic of the Co_3O_4 phase[24] and aligned with the XRD results, confirming the presence of Co_3O_4 in the composites. For the Co/Al_2O_3 catalyst, two peaks were observed at approximately 781.1 and 796.1 eV, corresponding to Co $2p_{3/2}$ and Co $2p_{1/2}$, respectively, while the two peaks at approximately 784.1 and 798.9 eV were their satellite peaks.[25] With the impregnation of Co/Al_2O_3 with K and Rb, the binding energies of both Co $2p_{3/2}$ and Co $2p_{1/2}$ peaks shifted to lower values, reflecting alterations in the catalyst's electronic environment and surface chemistry. This decrease in binding energy likely resulted from the promoters donating electron density to active metal sites or modifying the surface structure, thereby influencing the electron distribution around the atoms.[26]

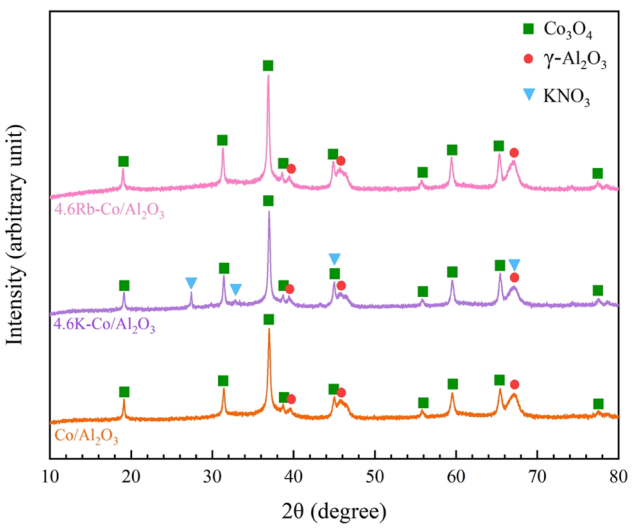

Fig. 2 XRD patterns of Co/Al_2O_3, 4.6K–Co/Al_2O_3, and 4.6Rb–Co/Al_2O_3 catalysts.

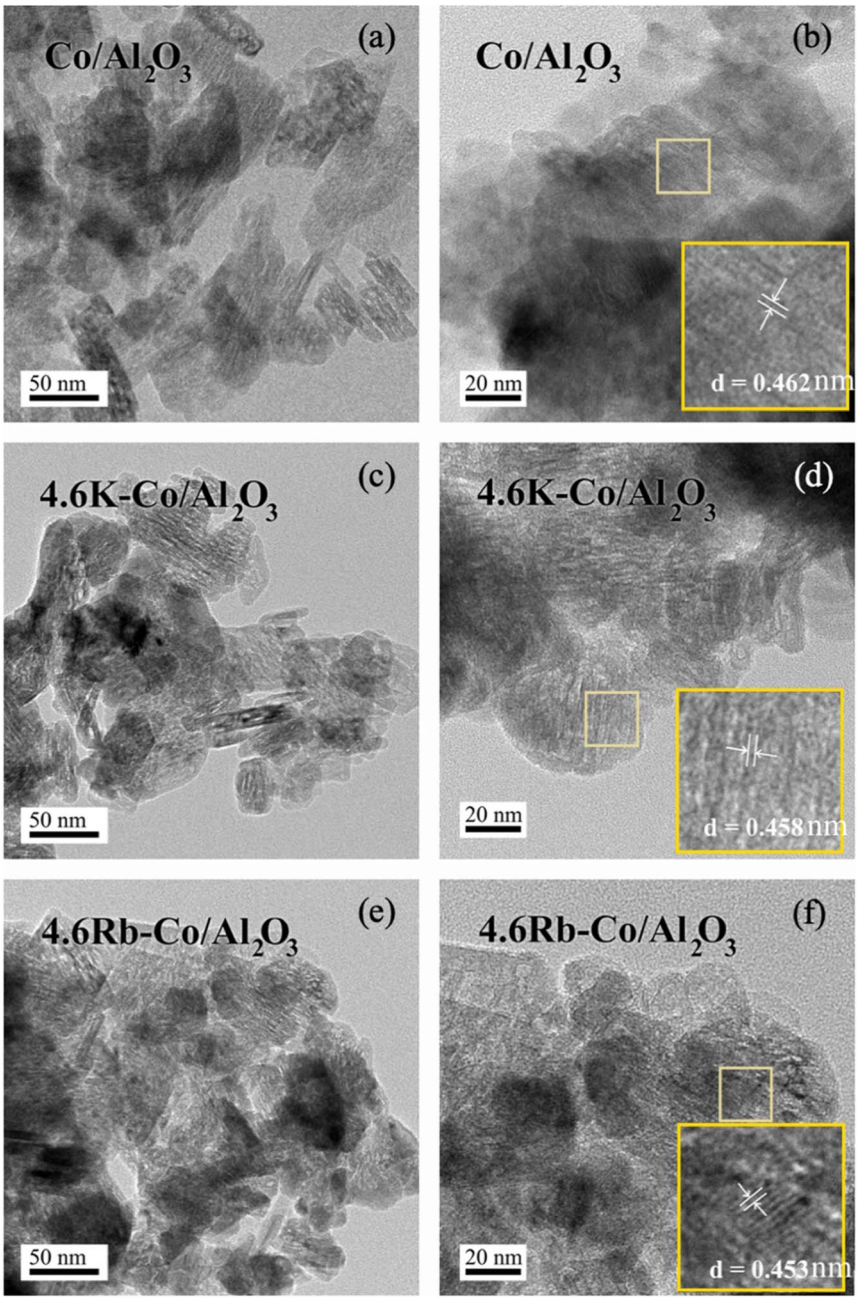

Fig. 3 HR–TEM images of (a and b) Co/Al_2O_3, (c and d) 4.6K–Co/Al_2O_3, and (e and f) 4.6Rb–Co/Al_2O_3.

For the 4.6K–Co/Al_2O_3 and 4.6Rb–Co/Al_2O_3 catalysts, there were shifts to lower binding energy values for both Co $2p_{3/2}$ and Co $2p_{1/2}$ compared to the catalyst without the dopant. The binding energy of each catalyst is summarized in Table S2.† These shifts to lower binding energies in the XPS spectra suggested an increase in electron density around the active sites, which promoted selective methane activation while reducing the likelihood of complete oxidation to CO and CO_2.[27] Consequently, the 4.6K–Co/Al_2O_3 catalyst showed better selectivity for C_2 hydrocarbons than the 4.6Rb–Co/Al_2O_3 catalyst.

3.2.5. Surface basicity of catalyst. The basicity of the catalysts was evaluated using CO_2-TPD desorption profiles over a temperature range of 200–800 °C, as shown in Fig. 8. The CO_2-TPD profiles for each catalyst could be divided into two categories: moderate basic sites (200–540 °C) and strong basic sites (560–800 °C). The desorption peaks for the Co/Al_2O_3, 4.6K–Co/Al_2O_3, and 4.6Rb–Co/Al_2O_3 catalysts were observed at 256.2, 400.1, and 413.2 °C, respectively, in the moderate temperature range, and at 600.0, 628.4, and 661.6 °C, respectively, in the strong temperature range. Surface basic sites, especially moderate basic sites, facilitate the adsorption and activation of CH_4 molecules, resulting in the formation of methyl radicals essential for C_2 hydrocarbon production.[5] Therefore, C_2 selectivity in the OCM reaction correlates with the estimated quantity

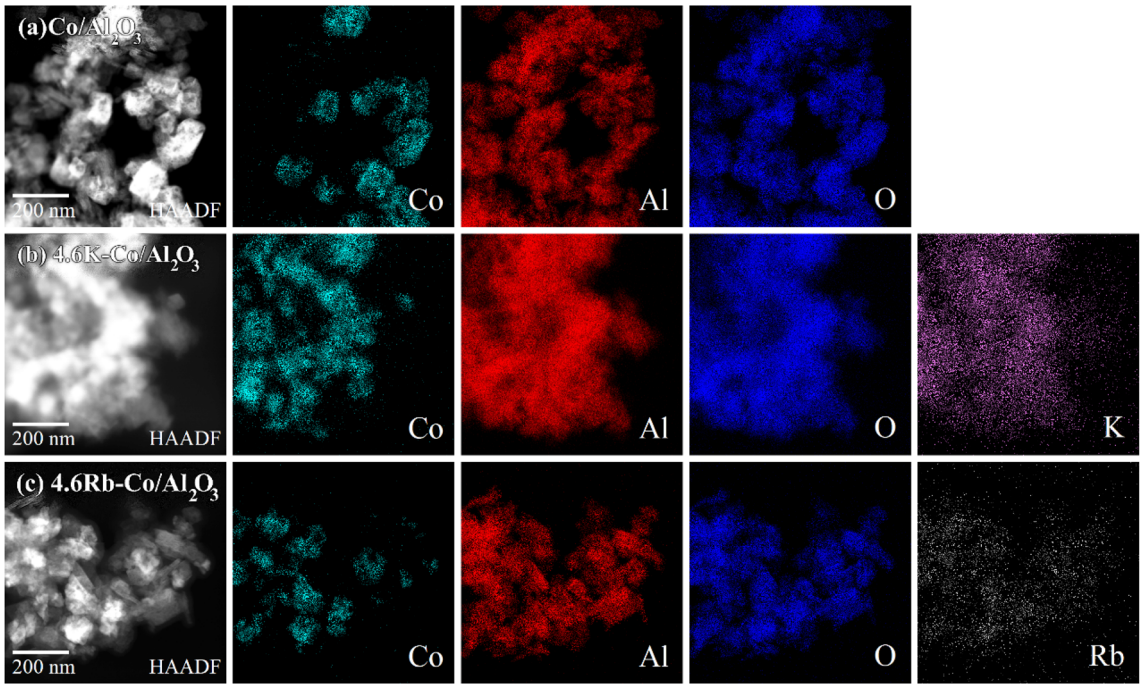

Fig. 4 Images of HAADF with EDS elemental mapping of (a) Co/Al_2O_3, (b) 4.6K–Co/Al_2O_3, and (c) 4.6Rb–Co/Al_2O_3.

of moderate basic sites, reflected by the area under the CO_2-TPD curve,[28,29] as summarized in Table 2. Compared to the Co/Al_2O_3 catalyst, the 4.6K–Co/Al_2O_3, and 4.6Rb–Co/Al_2O_3 catalysts had notable increases in the concentration of their moderate basic sites, attributed to the enhanced electron density on the surface introduced by these promoters, which effectively increased the overall basicity. The Co/Al_2O_3 catalyst had the lowest concentration of moderate basic sites, whereas the 4.6K–Co/Al_2O_3 catalyst had the highest concentration. This distribution was consistent with the catalytic performance results presented in Fig. 1, suggesting that the addition of K to the Co/Al_2O_3 catalyst enhanced the concentration of moderate basic sites, thereby facilitating the abstraction of H from CH_4 to form CH_3—an essential intermediate in the catalytic OCM reaction.[30]

3.2.6. Reduction properties of catalysts. The reducibility of the catalysts was assessed using H_2-TPR analysis, as shown in Fig. 9. Generally, the reduction of Co_3O_4 to metallic Co proceeds through two steps ($Co_3O_4 \rightarrow CoO \rightarrow Co^o$), where the reduction of Co_3O_4 generally takes place between 250 and 400 °C, followed by the reduction of CoO in the range of 400–600 °C.[31] In the current study, the H_2-TPR profiles for all catalysts displayed two reduction peaks: the first, corresponding to the reduction of Co_3O_4 to CoO, occurred at 402.2 °C, 343.5 °C, and 367.3 °C for the Co/Al_2O_3, 4.6K–Co/Al_2O_3, and 4.6Rb–Co/Al_2O_3 catalysts, respectively. The second peak, associated with reducing CoO to Co, appeared at 541.5 °C, 426.8 °C, and 557.9 °C for these

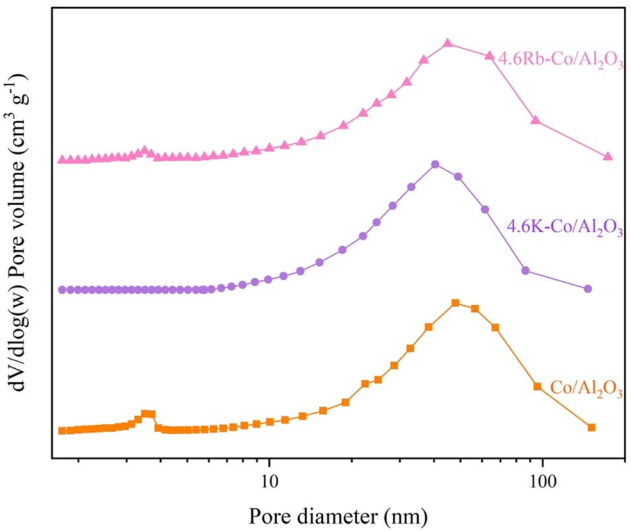

Fig. 5 Pore size distribution of Co/Al_2O_3, 4.6K–Co/Al_2O_3, and 4.6Rb–Co/Al_2O_3 catalysts.

Table 1 Surface area, pore volume, and pore diameter of each catalyst

Catalyst	Surface area ($m^2\ g^{-1}$)	Pore volume ($cm^3\ g^{-1}$)	Pore diameter (nm)
Co/Al_2O_3	1.21, 59.18	0.0001, 0.34	3.71, 47.90
4.6K–Co/Al_2O_3	27.80	0.27	40.46
4.6Rb–Co/Al_2O_3	4.90, 41.50	0.002,0.32	3.49, 44.89

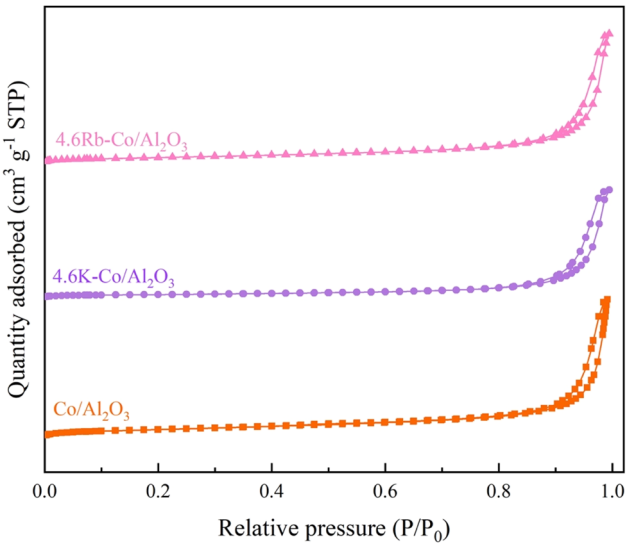

Fig. 6 N_2 adsorption–desorption isotherms of Co/Al_2O_3, 4.6K–Co/Al_2O_3, and 4.6Rb–Co/Al_2O_3 catalysts.

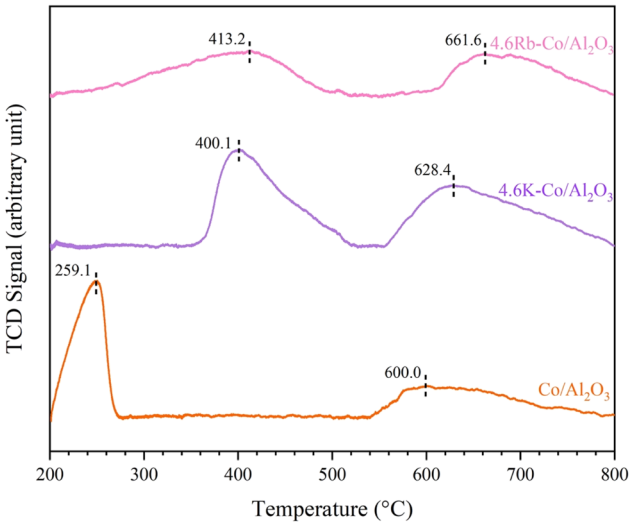

Fig. 8 CO_2-TPD profiles of Co/Al_2O_3, 4.6K–Co/Al_2O_3, and 4.6Rb–Co/Al_2O_3 catalysts.

catalysts, respectively. These results demonstrated that adding the promoters to the Co/Al_2O_3 catalyst impacted their reduction temperatures. The 4.6K–Co/Al_2O_3 catalyst had the lowest reduction temperatures, indicating the presence of highly reducible species and suggesting that the oxygen species could be replenished rapidly on the catalyst surface, ensuring a steady supply of reactive oxygen species (ROS) essential for methane activation.[32] Such a characteristic is crucial for sustaining catalytic activity and enhancing methane conversion efficiency. These findings aligned with the catalytic performance results, as the 4.6K–Co/Al_2O_3 catalyst had the highest activity among all the tested catalysts.

3.3 Optimal promoter weight percentage

According to Section 3.1, the Co/Al_2O_3 catalyst doped with K and Rb had high activity for the OCM reaction. This section describes the testing of different loadings (0.1, 0.5, 1.0, 2.0, 4.6, 6.0, 8.0, and 10.0 wt%) of these two promoters on the catalyst for the OCM reaction at atmospheric pressure and the reaction temperature of 490 °C. The activity results are shown in Fig. 10. The C_{2+} formation could be seen for the catalysts doped with K (0–0.5wt%) and Rb (0–2.0wt%). Then, the levels of catalytic performance (C_{2+} yield, C_{2+} selectivity, and CH_4 conversion) increased with an increasing percentage of promoters because the promoters formed active sites essential for methane activation and the ensuing coupling processes.[33] The highest performance percentages were 6.5% C_{2+} yields, 22.3% C_{2+} selectivity, and 29.5% CH_4 conversion for the 4.6K–Co/Al_2O_3 catalyst and 5.7% C_{2+} yield, 21.7% C_{2+} selectivity, and 26.3% CH_4 conversion for the 8Rb–Co/Al_2O_3 catalyst. However, excessive promoter loading resulted in aggregation or inadequate dispersion of active sites, reducing the effective surface area available for the reaction and potentially decreasing catalytic activity.[34] These testing results indicated that the most effective catalyst was the 4.6K–Co/Al_2O_3 catalyst.

Table 2 Distribution of the strength of basicity of catalysts

	Basicity amount (μmol g^{-1})	
Catalyst	Moderate basic sites (200–540 °C)	Strong basic sites (540–800 °C)
Co/Al_2O_3	0.83	0.63
4.6K–Co/Al_2O_3	1.37	1.22
4.6Rb–Co/Al_2O_3	0.98	0.72

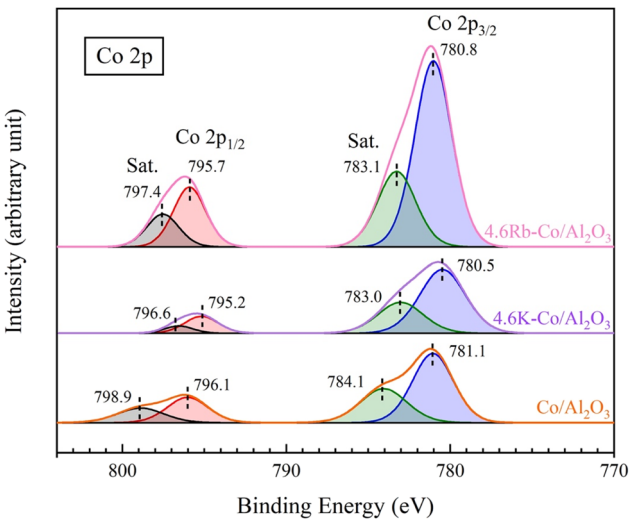

Fig. 7 XPS spectra of Co/Al_2O_3, 4.6K–Co/Al_2O_3, and 4.6Rb–Co/Al_2O_3 catalysts.

3.4 Optimal reaction temperature

To ensure a fair comparison based on the alkali metal content, the two catalysts were reformulated to possess equivalent molar

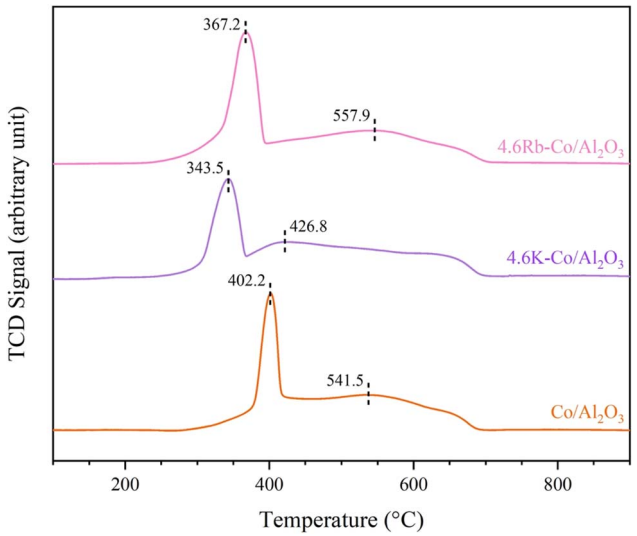

Fig. 9 H_2-TPR profiles of Co/Al_2O_3, 4.6K–Co/Al_2O_3, and 4.6Rb–Co/Al_2O_3 catalysts.

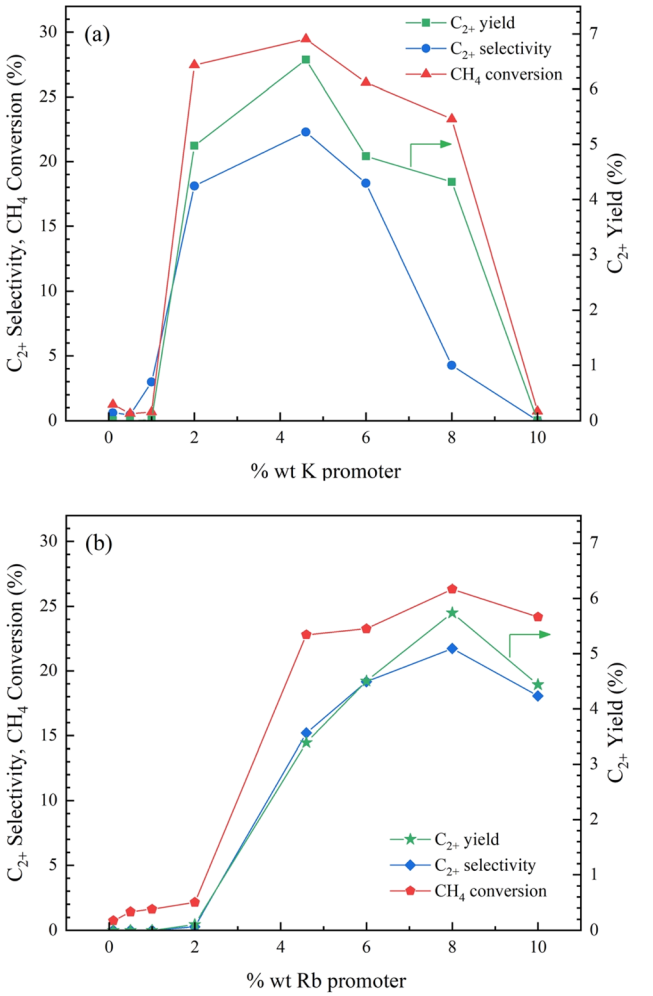

Fig. 10 Catalytic performance of (a) K–Co/Al_2O_3 catalyst and (b) Rb–Co/Al_2O_3 with varying weight percentages of promoter for OCM reaction. Reaction conditions: $CH_4 : O_2$ ratio = 2 : 1, catalyst weight = 40 mg, total feed flow rate = 40 mL min^{-1}, reactor temperature = 490 °C.

amounts of potassium and rubidium. This adjustment resulted in catalysts with revised weight loadings: 4.6K–Co/Al_2O_3 (*i.e.*, 2.05 molar of K on Co/Al_2O_3) and 10Rb–Co/Al_2O_3 (*i.e.*, 2.05 molar of Rb on Co/Al_2O_3). The impact of reaction temperature on catalytic performance was examined for both 4.6K–Co/Al_2O_3 and 10Rb–Co/Al_2O_3 catalysts over a temperature range of 440–740 °C, as shown in Fig. 11. The two catalysts exhibited similar performance. At low reaction temperatures (440 °C), CH_4 conversion was poor due to insufficient thermal energy to activate CH_4 molecules and promote coupling reactions, resulting in a low C_{2+} yield and selectivity. Then, the catalytic performance progressively increased with temperature up to the optimum reaction temperature, which was 640 °C for the 4.6K–Co/Al_2O_3 catalyst and 690 °C for the 10Rb–Co/Al_2O_3 catalyst, after which a decline was observed. Notably, 4.6K–Co/Al_2O_3 consistently demonstrated higher catalytic activity than 10Rb–Co/Al_2O_3. At 640 °C, the optimal performance of 4.6K–Co/Al_2O_3 achieved a C_{2+} yield of 8.1% with 24.0% C_{2+} selectivity and 32.1% CH_4 conversion, while the optimal performance of 10Rb–Co/Al_2O_3 occurred at 690 °C, resulting in a C_{2+} yield of 7.4% with 21.9% C_{2+} selectivity and 27.8% CH_4 conversion. Above the optimum temperature, both catalysts exhibited decreased catalytic performance, likely due to the increased formation of CO and CO_2 through the combustion of CH_4 and C_{2+} hydrocarbons. In summary, K-doped Co/Al_2O_3 exhibited superior performance in C_{2+} hydrocarbon formation compared to the Rb-doped counterpart at the same molar loading.

3.5 Catalytic stability of the 4.6K–Co/Al_2O_3 catalyst for the OCM reaction

The long-term stability of the 4.6K–Co/Al_2O_3 catalyst was assessed under continuous operation at 640 °C over a 24 h period, as illustrated in Fig. 12. At the beginning of the time-on-stream testing, the C_{2+} yield was 8.1%, with C_{2+} selectivity of 24.0% and a corresponding CH_4 conversion of 32.1%. As the reaction proceeded, a gradual change in performance was observed, followed by a relatively steady. After 24 h of testing, the catalyst maintained a C_{2+} yield of 8.2%, C_{2+} selectivity of 23.6%, and CH_4 conversion of 33.3%. According to these findings, the 4.6K–Co/Al_2O_3 catalyst shows excellent durability under reaction conditions, maintaining most of its initial activity over time.

The XRD analysis of the spent 4.6K–Co/Al_2O_3 catalyst, as shown in Fig. S2.† Peaks corresponding to Co_3O_4 and KNO_3 disappeared, while new reflections attributed to the $CoAl_2O_4$ spinel phase emerged prominently. This phase transformation likely occurred due to strong interactions between Co species and the Al_2O_3 support under high reaction temperature conditions (640 °C) and long operation time. The analysis shown in Fig. S3† was conducted to investigate potential coke formation on the catalyst after 24 h of use. A minor signal below 100 °C is likely due to moisture evaporation. Typically, coke formation is detected by TG–DTA analysis between 200 and 600 °C.[35]

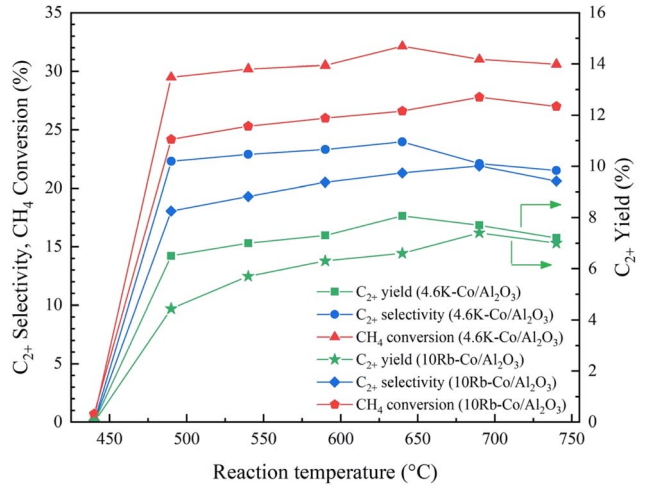

Fig. 11 Catalytic performance of the 4.6K–Co/Al_2O_3 and 10Rb–Co/Al_2O_3 catalyst with varying reaction temperatures for OCM reaction. Reaction conditions: $CH_4 : O_2$ ratio = 2 : 1, catalyst weight = 40 mg, total feed flow rate = 40 mL min^{-1}, reactor temperature = 440–740 °C.

However, in this case, no such signal was observed across that range, indicating that coke did not accumulate on the catalyst surface. Although XRD patterns revealed the presence of the $CoAl_2O_4$ phase in the spent catalyst, this had minimal influence on its behavior. Overall, the TG–DTA results confirmed the absence of coke, demonstrating that the catalyst maintained excellent performance under the tested conditions.

3.6 *In situ* DRIFTS analysis of 4.6K–Co/Al_2O_3 catalyst

In the OCM reaction, the electrophilic oxygen species, including the peroxide (O_2^{2-}) and superoxide (O_2^-) anions, play a critical role in enhancing CH_4 conversion and promoting C_2 selectivity during the OCM reaction.[36] The *in situ* DRIFTS analysis of the 4.6K–Co/Al_2O_3 catalyst, presented in Fig. 13, revealed a peak at 1014 cm^{-1}, attributed to surface O_2^- species.[30] The peaks at 1307 and 3012 cm^{-1} correspond to the presence of CH_4 in the gas phase, while the peak at 1356 cm^{-1} is associated with bidentate carbonate species (CO_3^{2-}).[37] Notably, no new surface carbonate species were detected after 30 min of reaction feed exposure. This suggested that the surface O_2^- species was regenerated by the O_2 present in the reaction feed. Additionally, a peak at 967 cm^{-1} was observed, signifying the formation of C_2H_4 on the catalyst surface under reaction conditions.[38] Furthermore, the catalyst had a peak at 2390 cm^{-1}, characteristic of adsorbed CO_2, and a peak at 1756 cm^{-1}, attributed to C=O stretching frequency, indicating CO formation during the OCM reaction.[37] A peak detected at 3630 cm^{-1} was assigned to the formation of O–H bonds. This suggests that a hydrogen atom from CH_4 was chemisorbed onto reactive oxygen sites on the catalyst surface through the formation of O–H bonds.[39] The results indicated that methane activation occurred through interaction with the active oxygen species on the 4.6K–Co/Al_2O_3 catalyst. This interpretation was consistent with other studies that identified oxygen as the active site for methane activation in gas–solid phase reactions.[40]

3.7 Proposed mechanism of the 4.6K–Co/Al_2O_3 catalyst for the OCM reaction

The analysis of the *in situ* DRIFTS results in Fig. 13, combined with insights from other studies on catalysts used in the OCM reaction, provided essential information for understanding the catalytic mechanism of the 4.6K–Co/Al_2O_3 catalyst. Initially, molecular O_2 dissociated on the catalyst surface, producing O_2^- species, which appeared at 1014 cm^{-1} in Fig. 13. It is also noted that the O_2^- band's constant intensity indicated that the consumption and regeneration of O_2^- proceed at a sufficiently rapid rate to achieve equilibrium at the reaction temperature.[36] Then, the O_2^- species extracted hydrogen from CH_4, forming methyl radicals ($^{\bullet}CH_3$) and surface hydroxyl groups (—OH),[39] which was confirmed by the *in situ* DRIFTS peak at 3630 cm^{-1}.

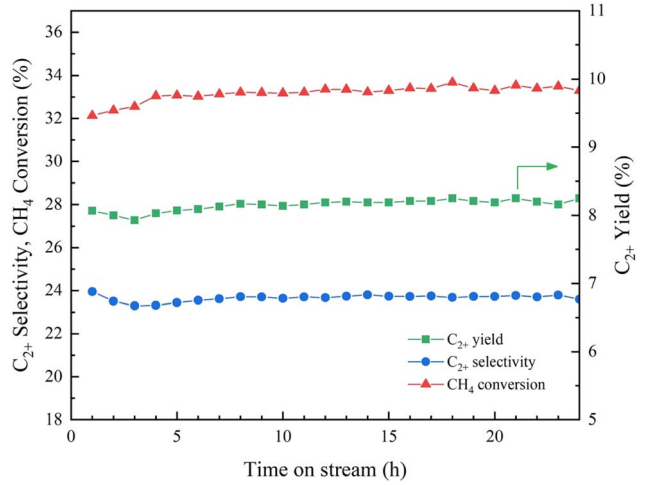

Fig. 12 The time-on-stream performance of the 4.6K–Co/Al_2O_3 catalyst over 24 h. Reaction conditions: $CH_4 : O_2$ ratio = 2 : 1, catalyst weight = 40 mg, total feed flow rate = 40 mL min^{-1}, reactor temperature = 640 °C.

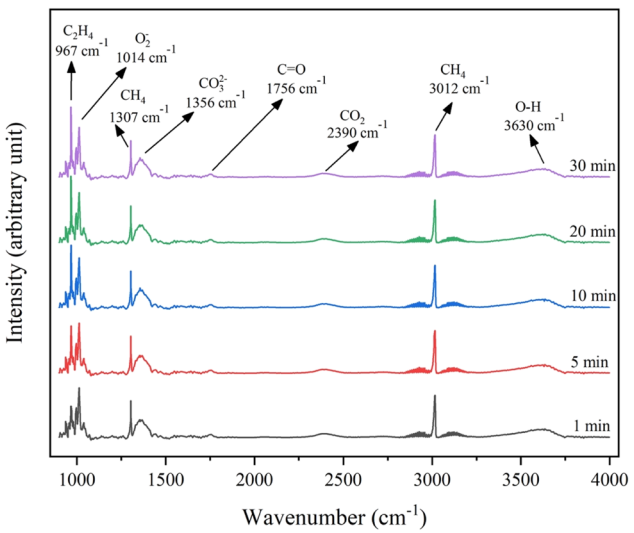

Fig. 13 *In-situ* DRIFTS spectra of the 4.6K–Co/Al_2O_3 catalyst.

The methyl radicals combined in the gas phase to form C_2H_6, which can subsequently produce C_2H_4, *via* dehydrogenation processes.[41] The synthesis of C_2H_4 on the catalyst surface was indicated by the peak at 967 cm^{-1}, with the concentration increasing with reaction time. The adsorbed –OH species may desorb from the surface as either $^{\bullet}OH$ or $^{\bullet}H$ radicals, which can further react to form H_2O. In addition, uncoupled radicals and hydrocarbons may undergo additional oxidation, forming CO and CO_2,[42] which appeared at 1756 and 2390 cm^{-1}, respectively.

However, a comparison between the mechanistic pathway proposed in this study and that of previously reported hybrid systems—specifically, the dual-layer catalyst comprising 5Ni/Al_2O_3 as the first layer and 4.6K–Co/Al_2O_3 as the second—reveals a fundamental distinction: in the earlier system, the reaction initiates as the reactant gases (CH_4 and O_2) pass through the first layer of the hybrid catalyst system, a portion of CH_4 is transformed into CO, CO_2, and H_2 *via* the partial oxidation of methane (POM) reaction. These products, particularly CO and H_2, serve as intermediate species for the subsequent Fischer–Tropsch synthesis occurring over the second catalyst layer. In the Fischer–Tropsch mechanism, which follows a chain-growth polymerization model, syngas components (CO and H_2) undergo surface dissociation into C, O, and H atoms during the initiation phase. A surface-bound C atom subsequently reacts with H atoms to generate CH_2 monomers, which then polymerize through successive coupling steps, ultimately leading to the formation of longer-chain hydrocarbons.

The 4.6K–Co/Al_2O_3 catalyst has several key components, each contributing to the catalytic process. The active components of this catalyst include K, Co, and Al_2O_3. The K component serves as a promoter, enhancing the number of basic sites on the catalyst that are essential for forming C_{2+} hydrocarbons.[43] Cobalt oxides, particularly Co_3O_4 with a spinel structure, are highly efficient at methane adsorption. Additionally, cobalt-based catalysts have major activity and selectivity in producing long-chain hydrocarbons.[44] Primarily, Al_2O_3 serves as a support material for the catalyst, owing to its advantageous properties, including a high surface area and well-distributed pore sizes, which facilitate superior metal dispersion and enhance catalyst stability.[45] In the current study, these factors likely contributed to the catalyst's high activity and exceptional performance at relatively low temperatures during the OCM reaction.

3.8 Comparative performance of 4.6K–Co/Al_2O_3 with other catalysts

Several catalysts investigated previously—particularly those comprising Na_2WO_4 in combination with Mn—have been recognized for their superior reactivity in the OCM process. To evaluate the performance of the optimized K–Co/Al_2O_3 catalyst developed in this study, a comparative analysis was conducted against selected representatives from this category, as illustrated in Fig. 14 and detailed in Table S3.† Reported performance for Na_2WO_4–Mn catalysts varies widely, with C_{2+} yields ranging from 0.2% to 31.6%, C_{2+} selectivities between 4.0% and 80.2%, and CH_4 conversion 1.0% to 45.4% at reaction temperatures of 650–850 °C. However, achieving both high conversion and high selectivity concurrently remains challenging. For commercial viability, a benchmark of at least 30% CH_4 conversion and 80% C_{2+} selectivities is typically required (as highlighted by the gray zone in Fig. 14). While a few catalysts exceed one of these thresholds, simultaneous attainment is rarely observed, indicating limitations in current materials. Notably, the K–Co/Al_2O_3 catalyst presented in this work attained 32.1% CH_4 conversion with 24.0% selectivity and 8.1%C_{2+} yield products at 640 °C, which lower than the operational temperatures of many high-performing systems. These findings underscore the importance of developing next-generation catalysts that can deliver high selectivity (>80%) while maintaining efficient CH_4 conversion (>30%), which is a critical direction for future innovation in OCM catalysis.

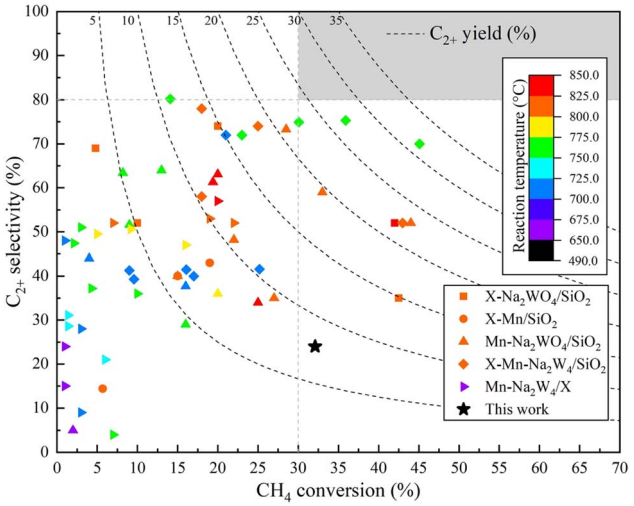

Fig. 14 Comparison of the catalyst developed in this study with other catalysts previously reported for the OCM reaction.

4. Conclusion

This study demonstrates the considerable influence of alkali metal promotion on the catalytic performance of Co/Al_2O_3 for the oxidative coupling of methane (OCM), a process crucial for sustainable methane utilization. Among the investigated alkali metal promoters (Li, Na, K, and Rb), K-promoted catalysts produced the most pronounced enhancement, with the optimized 4.6K–Co/Al_2O_3 catalyst achieving 8.1% C_{2+} yield, 24.0% C_{2+} selectivity, and 32.1% CH_4 conversion at 640 °C. Characterization revealed that K increased the surface basicity and modified the electronic environment of active sites, facilitating selective methane activation and suppressing complete oxidation to CO and CO_2. The mechanistic investigations, supported by *in situ* DRIFTS analysis, demonstrated that molecular O_2 dissociated on the catalyst, generating O_2^- species that extracted hydrogen from CH_4 to generate surface –OH groups and $^{\bullet}CH_3$, which subsequently recombined to produce C_2H_6 and dehydrogenated into C_2H_4. While Rb demonstrated potential, Li and Na had comparatively lower efficacy, emphasizing the

importance of promoter selection in optimizing catalytic performance. This research established that alkali metal-promoted Co/Al_2O_3, particularly the K-promoted variant, was a promising candidate for low-temperature OCM applications. These findings should provide valuable insights into the design of efficient, selective, and stable catalysts for the valorization of methane. Future research should focus on improving the properties of the catalyst and enhancing its performance to realize the full industrial potential of these systems.

Data availability

The datasets used and/or analyzed during the current study are available from the corresponding author upon reasonable request.

Author contributions

Sarannuch Sringam: Writing – original draft, writing – review & editing, methodology, investigation, validation, formal analysis, data curation. Punyanut Thansiriphat: Methodology, investigation. Thongthai Witoon: Methodology, investigation conceptualization. Waleeporn Donphai: Methodology, investigation. Metta Chareonpanich: Resources, conceptualization. Chularat Wattanakit: Resources, methodology. Hiesang Sohn: Resources, review & editing. Nevzat Yigit: Resources, methodology. Günther Rupprechter: Resources, conceptualization. Anusorn Seubsai: Writing – original draft, writing – review & editing, methodology, investigation, validation, formal analysis, data curation, supervision, project administration.

Conflicts of interest

There are no conflicts to declare.

Acknowledgements

Sringam, S. acknowledges the Center of Excellence on Petrochemical and Materials Technology for a PhD scholarship. This work was financially supported by the National Research Council of Thailand through the Fundamental Fund under the Kasetsart University Research and Development Institute (KURDI), Bangkok, Thailand, through Grant No. FF(KU)38.67; and the National Research Council of Thailand through the Research Team Promotion Grant/Senior Research Scholar (Grant No. N42A640324). Rupprechter, G. acknowledges support from the Austrian Science Fund (FWF; SFB TACO F81-P08).

References

1 C. Wei, M. Wang, Q. Fu, C. Dai, R. Huang and Q. Bao, *Atmos. Res.*, 2020, **235**, 104759.
2 C. Weng, X. Peng and Y. Han, *Adv. Appl. Microbiol.*, 2023, **124**, 119–146.
3 N. Sun, J. Zhang, L. Ling, R. Zhang, L. Jia, D. Li and B. Wang, *Appl. Catal.*, 2023, **650**, 118998.
4 H. Zhang, Y. Su, N. Kosinov and E. J. M. Hensen, *Chin. J. Catal.*, 2023, **49**, 68–80.
5 Y. Wang, X. Yang, F. Yin, K. Zhang, H. Guo, G. Wang, G. Jiang, C. Li and X. Zhu, *J. Energy Chem.*, 2022, **73**, 49–59.
6 C. A. Ortiz-Bravo, C. A. Chagas and F. S. Toniolo, *J. Nat. Gas Sci. Eng.*, 2021, **96**, 104254.
7 A. D. Talpade, G. Canning, J. Zhuchen, J. Arvay, J. Watt, J. T. Miller, A. Datye and F. H. Ribeiro, *Chem. Eng. J.*, 2024, **481**, 148675.
8 Z. Guo, W. Chen, Y. Song, X. Dong, G. Li, W. Wei and Y. Sun, *Chin. J. Catal.*, 2020, **41**, 1067–1072.
9 Y. Yu, K. Obata, W. J. Movick, S. Yoshida, J. Palomo, S. T. B. Lundin, A. Urakawa, S. M. Sarathy and K. Takanabe, *J. Catal.*, 2024, **432**, 115414.
10 E. G. Maulidanti, M. Awaji and K. Asami, *Gas Sci. Eng.*, 2023, **116**, 205057.
11 L. Xu, A. Zanina, K. Wu, J. Li, J. Chen, Y. Li, G. Jiang and E. V. Kondratenko, *Chem. Eng. J.*, 2023, **473**, 145372.
12 K. Zhao, J. Huang, Z. Huang, Y. Lin, M. Zheng, D. Song, A. Liu, X. Wang, A. Zheng and Z. Zhao, *J. Energy Inst.*, 2022, **105**, 273–281.
13 Y. Wang, W. Kong, Y. Fu, L. Zheng, B. Pan, H. Zhu, S. Li, J. Li, J. Zhang and Y. Sun, *J. Environ. Chem. Eng.*, 2024, **12**, 112757.
14 A. Zanina, D. Makhmutov and E. V. Kondratenko, *Catal. Today*, 2024, **439**, 114829.
15 P. Somchuea, T. Sukprom, S. Sringam, S. Ampansang, T. Witoon, M. Chareonpanich, K. Faungnawakij, G. Rupprechter and A. Seubsai, *Top. Catal.*, 2023, **66**, 1553–1568.
16 T. Sukprom, P. Somchuea, S. Sringam, T. Witoon, M. Chareonpanich, P. Iamprasertkun, K. Faungnawakij, G. Rupprechter and A. Seubsai, *React. Chem. Eng.*, 2023, **8**, 1868–1881.
17 J. Deng, P. Chen, S. Xia, M. Zheng, D. Song, Y. Lin, A. Liu, X. Wang, K. Zhao and A. Zheng, *Atmosphere*, 2023, **14**, 1538.
18 P. Kidamorn, W. Tiyatha, T. Chukeaw, C. Niamnuy, M. Chareonpanich, H. Sohn and A. Seubsai, *ACS Omega*, 2020, **5**, 13612–13620.
19 B. Małecka, A. Łącz, E. Drożdż and A. Małecki, *J. Therm. Anal. Calorim.*, 2015, **119**, 1053–1061.
20 H. Zhao, H. Song, F. Wang, Z. Miao and L. Chou, *Mol. Catal.*, 2020, **495**, 111141.
21 S. Alkhursani, N. Aldaleeli, A. Elbasiony, M. Ghobashy, S. Al-Gahtany and A. Sharshir, *Polym. Bull.*, 2024, **81**, 15841–15864.
22 J. Liu, J. Yue, M. Lv, F. Wang, Y. Cui, Z. Zhang and G. Xu, *Carbon Resour. Convers.*, 2022, **5**, 1–14.
23 L. Xu, J. Zhang, J. Ding, T. Liu, G. Shi, X. Li, W. Dang, Y. Cheng and R. Guo, *Minerals*, 2020, **10**, 72.
24 J. Yang, F. Wei, Y. Sui, J. Qi, Y. He, Q. Meng and S. Zhang, *RSC Adv.*, 2016, **6**, 61803–61808.
25 J. Acharya, B. G. S. Raj, T. H. Ko, M. S. Khil, H. Y. Kim and B. S. Kim, *Int. J. Hydrogen Energy*, 2020, **45**, 3073–3085.
26 Q. Zhang, L. Pastor-Pérez, W. Jin, S. Gu and T. R. Reina, *Appl. Catal., B*, 2019, **244**, 889–898.

27 Z. Wei, W. J. Movick, K. Obata, S. Yoshida, D. Asada, T. Ikeda, A. Nakayama and K. Takanabe, *J. Phys. Chem. C*, 2024, **128**, 12969–12977.
28 G. I. Siakavelas, N. D. Charisiou, A. AlKhoori, V. Sebastian, S. J. Hinder, M. A. Baker, I. V. Yentekakis, K. Polychronopoulou and M. A. Goula, *J. Environ. Chem. Eng.*, 2022, **10**, 107259.
29 S. Sringam, T. Witoon, C. Wattanakit, W. Donphai, M. Chareonpanich, G. Rupprechter and A. Seubsai, *Carbon Resour. Convers.*, 2024, 100261.
30 T. Wu, Y. Wei, J. Xiong, Y. Yang, Z. Wang, D. Han, Z. Zhao and J. Liu, *J. Energy Chem.*, 2024, **91**, 331–344.
31 N. F. Khairudin, M. Mohammadi and A. R. Mohamed, *Environ. Sci. Pollut. Res.*, 2021, **28**, 29157–29176.
32 H. Lin, Y. Liu, J. Deng, L. Jing and H. Dai, *Catalysts*, 2023, **13**, 427.
33 J. Hao, F. Cai, J. Wang, Y. Fu, J. Zhang and Y. Sun, *Chem. Phys. Lett.*, 2021, **771**, 138562.
34 A. H. K. Owgi, A. A. Jalil, M. A. A. Aziz, M. Alhassan, H. U. Hambali, W. Nabgan, R. Saravanan and A. H. Hatta, *Fuel*, 2023, **340**, 127592.
35 S. Ampansang, S. Sringam, P. Somchuea, T. Witoon, C. Wattanakit, M. Chareonpanich, H. Sohn and A. Seubsai, *Top. Catal.*, 2024, **67**, 394–408.
36 J. Xu, Y. Zhang, X. Xu, X. Fang, R. Xi, Y. Liu, R. Zheng and X. Wang, *ACS Catal.*, 2019, **9**, 4030–4045.
37 R. Singh Pal, S. Rana, S. Kumar Sharma, R. Khatun, D. Khurana, T. Suvra Khan, M. Kumar Poddar, R. Sharma and R. Bal, *Chem. Eng. J.*, 2023, **458**, 141379.
38 Y. Zhang, J. Xu, X. Xu, R. Xi, Y. Liu, X. Fang and X. Wang, *Catal. Today*, 2019, **355**, 518–528.
39 T. Shen, Z. Wang, S.-M. Xu, X. Sun, G. Liu, S. Bai, J. Li, Z. Song, L. Zheng and Y.-F. Song, *Cell Rep. Phys. Sci.*, 2023, **4**, 101478.
40 Y. Wang, B. Wang, S. Sourav, R. Batchu, Z. Fang, M. R. Kunz, G. Yablonsky, E. Nikolla and R. Fushimi, *Catal. Today*, 2023, **417**, 113739.
41 D. Kiani, S. Sourav, J. Baltrusaitis and I. E. Wachs, *ACS Catal.*, 2019, **9**, 5912–5928.
42 T. Chukeaw, W. Tiyatha, K. Jaroenpanon, T. Witoon, P. Kongkachuichay, M. Chareonpanich, K. Faungnawakij, N. Yigit, G. Rupprechter and A. Seubsai, *Process Saf. Environ. Prot.*, 2021, **148**, 1110–1122.
43 Y. Xie, W. Wang, J. Cui, H. Li, K. Cheng, Q. Zhang and Y. Wang, *Chem. Eng. Sci.*, 2024, **294**, 120119.
44 S. Guo, Z. Ma, J. Wang, B. Hou, L. Jia, B. Wang and D. Li, *Fuel*, 2021, **292**, 120398.
45 S. Khan, S. S. Shah, N. K. Janjua, A. B. Yurtcan, M. T. Nazir, K. M. Katubi and N. S. Alsaiari, *Chemosphere*, 2023, **315**, 137659.